



ORIGINAL PAPER

Bing Chen · Tiantang Yu · Sundararajan Natarajan ·  
Qing Zhang · Tinh Quoc Bui

# Numerical simulation for quasi-static crack growth and dynamic crack branching by coupled state-based PD and XFEM

Received: 1 November 2022 / Revised: 13 March 2023 / Accepted: 23 April 2023 / Published online: 9 May 2023  
© The Author(s), under exclusive licence to Springer-Verlag GmbH Austria, part of Springer Nature 2023

**Abstract** This paper presents a novel framework combining the state-based peridynamics (SBPD) with the extended finite element method (XFEM) for crack propagation in two-dimensional solids. Numerical examination is conducted fulfilling both the quasi-static and time-dependent loading conditions. The computational domain is partitioned into two regions: (a) SPBD region: the vicinity of crack tips and potential region where the crack is likely to propagate, and (b) XFEM region: the area behind the crack tip and the rest of the body. The salient features of the developed framework include: (a) avoiding requirement of a priori knowledge of enrichment functions like the conventional XFEM; (b) without fracture criteria for crack propagation; (c) no restriction on the value of Poisson's ratio like the bond-based peridynamics; and (d) higher computational efficiency than the pure peridynamics. The efficiency and accuracy of the proposed framework are systematically demonstrated through benchmark examples involving quasi-static crack growth and dynamic crack branching problems.

## 1 Introduction

Peridynamics (PD) [1] based on a non-local theory uses integro-differential equations rather than differential equations to describe the governing equations of motion. This facilitates easy modelling of problems involving discontinuous and/or singular solutions without any additional pre- and post-processing techniques. This is in contrast to conventional approaches that require conforming mesh with special elements, viz., singular elements or enrichment techniques to capture the necessary physics of the problem. Further, the conventional approaches require additional post-processing techniques to estimate the fracture parameters and a fracture criteria for the discontinuous surface to evolve.

Since its inception, the PD theory has been applied to wider variety of problems in science and engineering [2–9]. As with any other numerical method, the PD theory has its share of difficulties. The biggest disadvantage

---

B. Chen · T. Yu (✉) · Q. Zhang  
College of Mechanics and Materials, Hohai University, Nanjing 211100, People's Republic of China  
E-mail: tiantangyu@hhu.edu.cn

S. Natarajan  
Department of Mechanical Engineering, Indian Institute of Technology Madras, Chennai 600036, India

T. Q. Bui (✉)  
Duy Tan Research Institute for Computational Engineering (DTRICE), Duy Tan University, 6 Tran Nhat Duat, Dist. 1,  
Ho Chi Minh City, Viet Nam  
E-mail: tinh.buiquoc@gmail.com, buiquoctinh@duytan.edu.vn

T. Q. Bui  
Faculty of Civil Engineering, Duy Tan University, Da Nang City 550000, Viet Nam

of the PD is the low computational efficiency, which limits the engineering application of this method. Hence, improving the computational efficiency of PD has been concerning in the scientific community and the recent focus amongst the researchers is on improving the computational efficiency of the framework [10–14].

The local theory-based numerical methods (e.g. the finite element method (FEM), extended FEM (XFEM), boundary element method (BEM), isogeometric analysis (IGA), meshfree method, etc.) have high computational efficiency. The coupling of PD and the local theory-based numerical method becomes an effective technique to enhance the computational efficiency of PD. PD has been coupled with FEM [15–19], BEM [20–22], IGA [23–25], and XFEM [26–29], to name a few.

Amongst aforementioned approaches, coupling with the XFEM has gained attention. This is because the XFEM does not require the discontinuities to conform to the background discretization, but requires a fracture criteria for modelling crack propagation. So a combination of the PD theory with the XFEM is an ideal choice, especially for three-dimensional problems with complex crack patterns and morphologies. The coupling of the PD with the XFEM yields a framework that shares the advantages of both the methods, thus facilitating simulation of fracture process of large-scale engineering structures.

Recently, the present authors developed a coupling approach that combines the PD with the XFEM for three-dimensional crack propagation fulfilling both the quasi-static and dynamic loadings [30]. In our previous study, the bond-based PD [31] was used, and so Poisson's ratio is limited to  $\frac{1}{4}$  under plane strain and 3D conditions and  $\frac{1}{3}$  under plane stress condition. Existing coupling approaches between the PD and the XFEM are all based on the bond-based PD [26–29]. To improve the modelling capability and to relax the constraint on Poisson's ratio, Silling [32] proposed a state-based peridynamics theory (SBPD) that is suitable for any material. Hence, the primary objective of this work is to develop a coupling strategy between the SBPD and the XFEM method. To facilitate easy discussion, we have restricted the focus to two-dimensional crack propagation problems under quasi-static and dynamic loading conditions. This is accomplished by dividing the domain into two regions, namely, SBPD region, which is used in the crack tip and the potential crack growth domain, thus the fracture criteria for crack growth is not required, and the XFEM region, which is applied in the rest of the computational domain to reduce the computational cost and improve the computational efficiency. The accuracy and efficiency of the proposed coupled framework are demonstrated through a few standard problems involving quasi-static crack propagation and dynamic crack branching. The coupling approach based on the state-based PD with the XFEM method has not been found in the literature, and this study is an extension of our previous work, i.e. relaxing the constraint on Poisson's ratio.

The manuscript is organized as follows. The coupling scheme between the state-based PD and the XFEM is presented in Sect. 2, and its accuracy verification is discussed in Sect. 3. Several 2D crack propagation and dynamic crack branching simulations are discussed in Sect. 4. Some major conclusions are given in Sect. 5.

## 2 Formulation for coupling SBPD and XFEM

The main idea of coupling the SBPD and the XFEM is to capture the physics in the vicinity of the crack tip and potential crack propagation regions using the PD, and the rest of the computational domain is modelled using the XFEM.

The coupled method possess the advantages of the SBPD for the crack propagation and the XFEM for describing the discontinuous displacements independent of the underlying background discretization. Thus, the coupled method enhances the computation efficiency in comparison with the conventional SBPD and avoids the need for a fracture criteria for crack propagation. A coupling scheme between the SBPD and the XFEM is presented in this section.

### 2.1 The state-based peridynamics

In PD, a solid consists of some material points, and  $\mathbf{x}$ , the material point, interacts with other material points within its horizon  $H_{\mathbf{x}}$  with horizon radius  $\delta$ . Under the external loading condition, the displacements of the material points  $\mathbf{x}_i$  and  $\mathbf{x}_j$  in the initial configuration are  $\mathbf{u}(\mathbf{x}_i)$  and  $\mathbf{u}(\mathbf{x}_j)$ , and the locations in the deformed configuration are  $\mathbf{y}_i$  and  $\mathbf{y}_j$ , respectively. In the SBPD, the force density vectors have unequal magnitudes and are parallel to the relative position vector in the deformed state, and the balance of angular momentum can be satisfied. Assuming small deformation, the equations of motion in discrete form for a material point  $\mathbf{x}_i$  at time

$t$  is expressed as [33]:

$$\begin{aligned} & \sum_{j=1}^N \psi_{ij} \left( \frac{4b\delta V_j V_i}{\|\mathbf{x}_j - \mathbf{x}_i\|} (\mathbf{u}_i - \mathbf{u}_j) + \sum_{m=1}^N \psi_{im} \frac{2ad^2\delta^2 V_m V_j V_i}{\|\mathbf{x}_j - \mathbf{x}_i\| \|\mathbf{x}_m - \mathbf{x}_i\|} (\mathbf{u}_i - \mathbf{u}_m) \right. \\ & \left. + \sum_{n=1}^N \psi_{jn} \frac{2ad^2\delta^2 V_n V_j V_i}{\|\mathbf{x}_j - \mathbf{x}_i\| \|\mathbf{x}_n - \mathbf{x}_j\|} (\mathbf{u}_j - \mathbf{u}_n) \right) + \rho \ddot{\mathbf{u}}_i V_i = \mathbf{b}(\mathbf{x}_i) V_i \end{aligned} \quad (1)$$

where  $N$  is the number of material points within the horizon of  $\mathbf{x}_i$  and  $\rho$  denotes the mass density.  $\ddot{\mathbf{u}}_i$ ,  $V_i$  and  $\mathbf{b}(\mathbf{x}_i)$  are the acceleration vector, the volume and the body force density of a material point  $\mathbf{x}_i$ , respectively.  $\psi_{ij}$  is the status function and  $a$ ,  $b$  and  $d$  are the PD parameters. For 2D problem, the PD parameters are defined as [34]:

$$a = \frac{1}{2}(k - 2\mu), \quad b = \frac{6\mu}{\pi h \delta^4}, \quad d = \frac{2}{\pi h \delta^3} \quad (2)$$

where  $h$  is the thickness,  $k$  is  $\frac{E}{2(1-\nu)}$  for plane stress and  $\frac{E}{2(1+\nu)(1-2\nu)}$  for plane strain,  $\mu = \frac{E\nu}{2(1+\nu)}$ ,  $E$  and  $\nu$  are Young's modulus and Poisson's ratio.

It is assumed that two material points  $\mathbf{x}_i$  and  $\mathbf{x}_j$  are connected by a bond and the stretch  $s_{ij}$  is computed by:

$$s_{ij} = \frac{\|\mathbf{y}_j - \mathbf{y}_i\| - \|\mathbf{x}_j - \mathbf{x}_i\|}{\|\mathbf{x}_j - \mathbf{x}_i\|} \quad (3)$$

where,  $\psi_{ij} = 1$  for  $s_{ij} < s_c$ , 0 for  $s_{ij} \geq s_c$ ,  $s_c$  is the critical bond stretch. For 2D problem, the critical bond stretch is defined as [34]:

$$s_c = \sqrt{\frac{G_c}{\left(\frac{6}{\pi}\mu + \frac{16}{9\pi^2}(k - 2\mu)\right)\delta}} \quad (4)$$

where  $G_c$  is the macroscopic critical energy release rate.

Equation (1) can be written in matrix form as follows:

$$\begin{aligned} & \sum_{j=1}^N \psi_{ij} \left( \mathbf{k}_{ij}^{11} \mathbf{u}_i + \mathbf{k}_{ij}^{12} \mathbf{u}_j + \sum_{m=1}^N \psi_{im} \left( \bar{\mathbf{k}}_{im}^{11} \mathbf{u}_k + \bar{\mathbf{k}}_{im}^{12} \mathbf{u}_i \right) \right. \\ & \left. + \sum_{n=1}^N \psi_{jn} \left( \bar{\mathbf{k}}_{in}^{11} \mathbf{u}_n + \bar{\mathbf{k}}_{ij}^{12} \mathbf{u}_j \right) \right) + \mathbf{m}_i^{PD} \ddot{\mathbf{u}}_i = \mathbf{R}_i^{PD} \end{aligned} \quad (5)$$

with

$$\mathbf{k}_{ij}^{PD} = \frac{4b\delta V_i V_j}{\|\mathbf{x}_j - \mathbf{x}_i\|} \begin{bmatrix} l^2 & lm & -l^2 & -lm \\ lm & m^2 & -lm & -m^2 \\ -l^2 & -lm & l^2 & lm \\ -lm & -m^2 & lm & m^2 \end{bmatrix} = \begin{bmatrix} \mathbf{k}_{ij}^{11} & \mathbf{k}_{ij}^{12} \\ \mathbf{k}_{ij}^{21} & \mathbf{k}_{ij}^{22} \end{bmatrix} \quad (6)$$

$$\bar{\mathbf{k}}_{im}^{PD} = \frac{2\delta^2 d^2 a}{\|\mathbf{x}_m - \mathbf{x}_k\| \|\mathbf{x}_j - \mathbf{x}_i\|} \begin{bmatrix} l^2 & lm & -l^2 & -lm \\ lm & m^2 & -lm & -m^2 \\ -l^2 & -lm & l^2 & lm \\ -lm & -m^2 & lm & m^2 \end{bmatrix} = \begin{bmatrix} \bar{\mathbf{k}}_{im}^{11} & \bar{\mathbf{k}}_{im}^{12} \\ \bar{\mathbf{k}}_{im}^{21} & \bar{\mathbf{k}}_{im}^{22} \end{bmatrix} \quad (7)$$

$$\bar{\mathbf{k}}_{jn}^{PD} = \frac{2\delta^2 d^2 a}{\|\mathbf{x}_n - \mathbf{x}_j\| \|\mathbf{x}_j - \mathbf{x}_i\|} \begin{bmatrix} l^2 & lm & -l^2 & -lm \\ lm & m^2 & -lm & -m^2 \\ -l^2 & -lm & l^2 & lm \\ -lm & -m^2 & lm & m^2 \end{bmatrix} = \begin{bmatrix} \bar{\mathbf{k}}_{jn}^{11} & \bar{\mathbf{k}}_{jn}^{12} \\ \bar{\mathbf{k}}_{jn}^{21} & \bar{\mathbf{k}}_{jn}^{22} \end{bmatrix} \quad (8)$$

where  $\mathbf{R}_i^{PD} = \mathbf{b}(\mathbf{x}_i) V_i$ ,  $\mathbf{m}_i^{PD} = \rho V_i$ ,  $l = \frac{x_j - x_i}{\|\mathbf{x}_j - \mathbf{x}_i\|}$  and  $m = \frac{y_j - y_i}{\|\mathbf{x}_j - \mathbf{x}_i\|}$ .

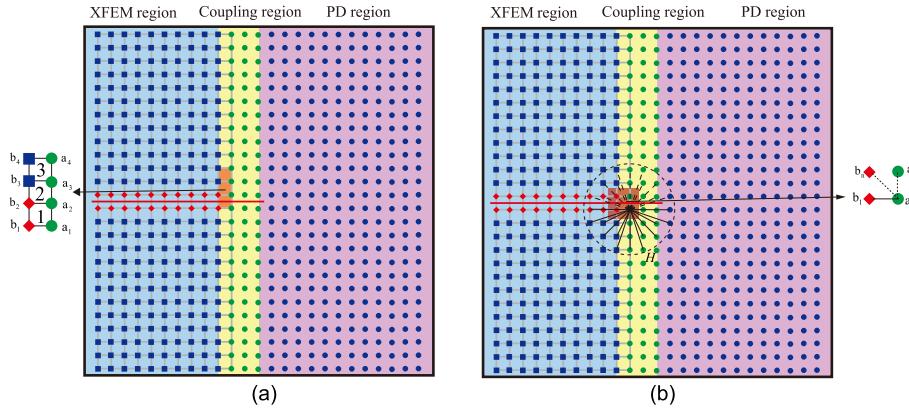


Fig. 1 Region divisions, **a** coupling elements, and **b** coupling bonds

2.2 The extended finite element method

In XFEM setting, the standard finite element approximation is augmented by some special functions based on the partition of unity. This process is commonly referred to as *enrichment* strategy. This facilitates the representation of the discontinuities independent of the underlying background mesh. For a domain with a discontinuous surface, the enriched displacements approximation is expressed as [35]

$$\mathbf{u} = \sum_{i \in N^a} N_i(\mathbf{x}) \mathbf{u}_i + \sum_{m \in N^s} N_m(\mathbf{x}) [\phi(\mathbf{x}) - \phi(\mathbf{x}_m)] \mathbf{a}_m \tag{9}$$

where  $\mathbf{u}_i$  and  $\mathbf{a}_m$  are the nodal displacements and enriched variables, respectively.  $N^a$  is the set of all nodes in the considered domain, while  $N^s$  is the set of enriched nodes.  $N_i(\mathbf{x})$  and  $N_m(\mathbf{x})$  denote the standard finite element shape functions. In this work, the enrichment function  $\phi$  is +1 on one side of the crack and -1 on the other side. The corresponding weak form and discretized form are obtained by employing the standard Bubnov-Galerkin method. For additional details, interested readers are referred to [36] and references therein.

2.3 The coupling approach between SBPD and XFEM

A schematic of the computational domain partitioned into regions, viz., SPBD region, XFEM region and an overlapping region is shown in Fig. 1. The original crack without the crack tip is considered as a part of the XFEM region. The crack tip and the potential crack propagation region are included in the SBPD region and in the overlapping region, both the descriptions coexist. An overlapping region is required because the XFEM region is modelled using the local theory and the PD region is modelled using the non-local theory. In Fig. 1, ‘blue’ square and ‘red’ diamond represent the standard and the enriched nodes in XFEM region, while the ‘blue’ circle represents the standard PD nodes, and the ‘green’ circle denotes the coupled nodes.

In the coupling region, the XFEM element contains PD material points to form a coupling element, and the PD material points in the coupling region also interacts with the XFEM nodes in the horizon to form a coupling bond. In the coupling element, all nodes (including PD material points and XFEM nodes) only exert force on the XFEM nodes. In the coupling bond, all nodes (including PD material points and XFEM nodes) only exert force on PD material points. Aforementioned definition of coupling element and bond ensures that the information between the XFEM region and the PD region is transferred seamlessly and smoothly.

In the coupling region, XFEM nodes in the coupling element interact with all surrounding nodes (including nodes that belong to the XFEM region and material points of PD region). Using the above coupling element treatment scheme, the relevant terms of PD material points in the stiffness and mass matrices of the coupling element are zero. To present the displacement of the XFEM accurately, the terms corresponding to the enriched variables (including XFEM nodes and PD material points) in the stiffness and mass matrices of the coupling element are retained. A material point in the coupling region interacts with all nodes in its horizon (including XFEM nodes and PD material points). According to the processing method of coupling bond, the material points are set to zero for the term corresponding to XFEM nodes in the stiffness and mass matrices.

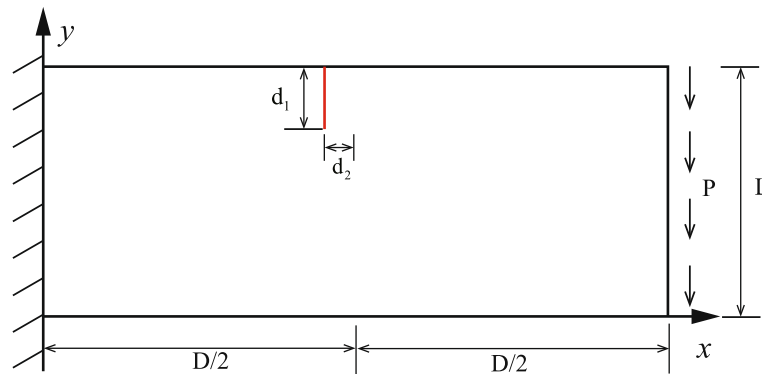


**Fig. 2** Schematic illustration of the cantilever beam with an edge crack

With  $\delta$  denoting the global nodal variable vector and  $F$  being the global external nodal force vector, the governing equation of the coupling XFEM-PD is obtained as follows:

$$M\ddot{\delta} + K\delta = F \tag{10}$$

where  $K$  and  $M$  are the global stiffness and mass matrices, respectively. Through the assembly of stiffness and mass matrices of all XFEM elements and PD nodes, the global stiffness and mass matrices are thus obtained.

In this study, PD region denotes the vicinity of crack tips and potential region where the crack is likely to propagate, and XFEM region is the area behind the crack tip and the rest of the body. Thus PD theory is not used in the whole computational domain, so the role of XFEM is to reduce the computational cost and improve the computational efficiency. In order to simplify the problem, the PD region remains unchanged in this study, in fact a variable PD region can further save time. It is noted that the coupling region can be a free-shape zone. The coupling scheme and numerical implementation are the same as those given in Ref. [30].

In the coupled SBPD and FEM, the computational domain is also divided two regions, namely, SBPD region and FEM region. The FEM region in the coupled SBPD and FEM is the XFEM region in the coupled SBPD and XFEM. In addition, the FEM region contains cracks. In the FEM, element edges should be aligned with crack faces, while meshes are independent of the internal geometry and physical interfaces (such as cracks) in the XFEM, as shown in Fig. 1. It is obvious that the XFEM is more convenient than the FEM for modelling cracks. Hence, the XFEM is adopted instead of the ordinary FEM in the cracked domain in this study, i.e. the coupled SBPD and XFEM is used instead of the coupled SBPD and FEM.

### 3 Accuracy verification

To verify the accuracy of the proposed framework, a cantilever beam with an edge crack under a uniformly distributed shearing force is considered, as shown in Fig. 2. The length  $D$  of the cantilever beam is 50 mm, the height  $L$  is 20 mm, the crack length  $d_1$  is 5 mm, and  $d_2$  is 2.5 mm. The shear force on the right end is  $P = -1$  KN/m. Following material properties are considered for this study: Young’s modulus  $E = 1$  GPa, Poisson’s ratio  $\nu = 0.2$ . A state of plane stress condition is assumed. In order to investigate the influence of region division on the accuracy, two different region division schemes are adopted, as shown in Fig. 3. In Fig. 3,  $L_1 = 3.5$  mm,  $L_2 = 1.5$  mm,  $L_3 = 15$  mm,  $L_4 = 20$  mm,  $L_5 = 1.5$  mm,  $L_6 = 15$  mm, and  $L_7 = 13.5$  mm. The grid is evenly divided with a spacing of  $\Delta x = 0.5$  mm. In the PD region, the size of horizon  $\delta = 3\Delta x$  is used.

The horizontal displacements on  $y = \frac{L}{2}$  and the vertical displacements on  $x = \frac{D}{2}$ , respectively, and the results obtained with XFEM are also given in Figs. 4 and 5 for comparison. From Figs. 4 and 5, it is found that (1) the displacements obtained by the coupling model with the two region division schemes match well with the results obtained by XFEM, which shows that the coupling model has good solution accuracy, and (2) the results of the coupling model with the two region division schemes are almost the same, which show that the influence of region division is small.

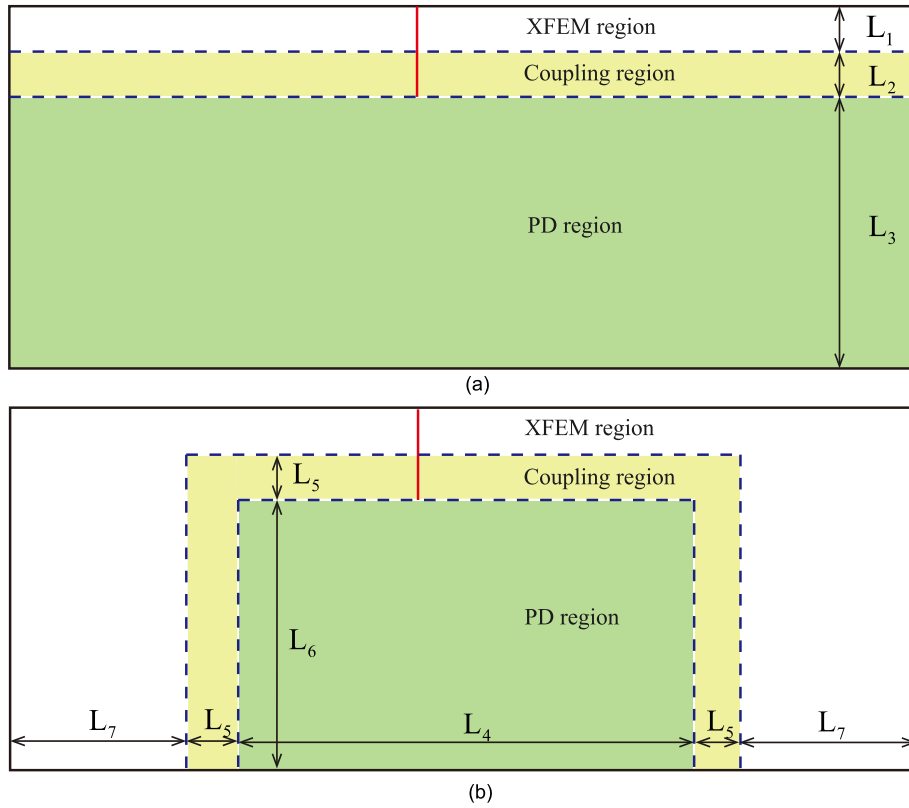


**Fig. 3** Two region division schemes of the cantilever beam, **a** coupling model 1, and **b** coupling model 2

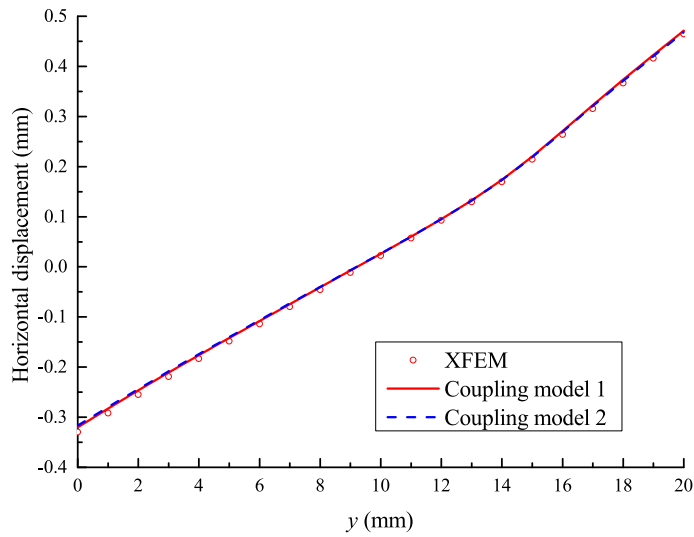


**Fig. 4** Comparison on horizontal displacements on  $x = \frac{D}{2}$

**4 Numerical examples**

To show the performance of the present framework for 2D crack propagation problem, four numerical examples, viz., two for quasi-static boundary conditions and two for dynamic loading, are considered. For all the numerical examples, a state of plane stress condition is assumed unless mentioned otherwise. A structured 4-node quadrilateral element is used.

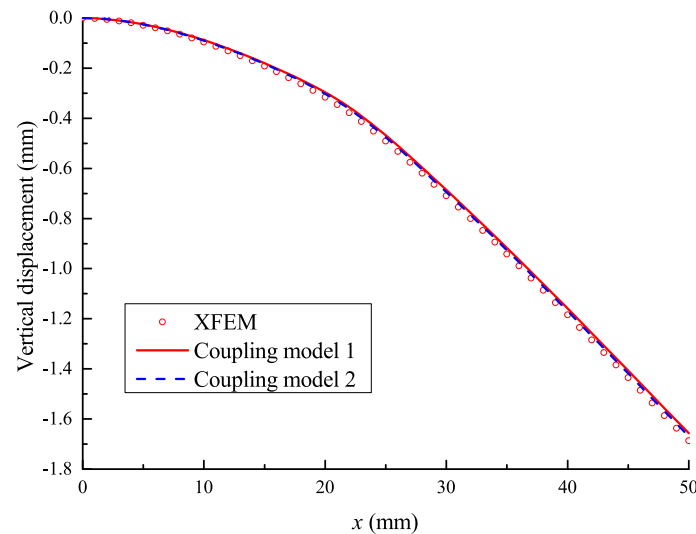


**Fig. 5** Comparison on vertical displacements  $y = \frac{L}{2}$

#### 4.1 Quasi-static analysis: Mode-I crack propagation in an edge-cracked plate

The first example deals with a square plate with an edge crack under uniaxial tension as depicted in Fig. 6. The plate length is  $L = 0.1$  m, the thickness is  $t = 1$  mm, and the crack length is 50 mm. The top and the bottom edges of the plate are subjected to Dirichlet boundary conditions. The material properties considered for this example include: Young's modulus is  $E = 35,770$  MPa, Poisson's ratio is  $\nu = 0.38$ , and critical energy release rate is  $G_{IC} = 9.8$  N/m. The computational domain is discretized with a uniform grid size of  $\Delta x = 1$  mm. In the PD region, the size of horizon is  $\delta = 3\Delta x$ .

The region division is shown in Fig. 7,  $L_1 = 53$  mm,  $L_2 = 20$  mm,  $L_3 = 3$  mm and  $L_4 = 34$  mm. The Dirichlet boundary conditions are imposed incrementally with  $\Delta u_y = 5 \times 10^{-5}$  mm before fracture. Once the bond is broken, the displacement increment is reduced to  $\Delta u_y = 5 \times 10^{-6}$  m, until crack propagation is completed. The crack growth process is shown in Fig. 8, in which Fig. 8a–c are the crack propagation processes obtained by the coupling method and Fig. 8d–f are the crack propagation processes simulated by the pure PD. It can be found that the crack path simulated by the two methods are consistent, and conform to the mode-I crack propagation path. When the displacement increment reaches 0.0041 mm, the crack starts propagation, and the plate is snapped when the displacement increment reaches 0.005 mm. The calculation time estimated for the coupling method and the pure PD is 2543 s and 3564 s, respectively, and this means that the coupling method has much higher efficiency than the pure PD.

#### 4.2 Quasi-static analysis: mixed-mode crack propagation in a central-cracked-square plate

Mixed-mode crack propagation in a square plate with a central crack as shown in Fig. 9 is considered. The side length of the plate is  $2W = 150$  mm, the plate thickness is  $t = 5$  mm, the crack length is  $2a = 45$  mm, and the inclined angle of the crack is  $\alpha$ . There are two loading circular holes on the upper and lower corners,  $r = 4$  mm, and  $d = 25$  mm. The material parameters are: Young's modulus  $E = 2940$  MPa, Poisson's ratio  $\nu = 0.38$ , and average fracture toughness  $K_{IC} = 1.33$  MPa $\sqrt{\text{m}}$ . The conversion relationship between energy release rate  $G_{IC}$  and average fracture toughness  $K_{IC}$  is  $G_{IC} = \frac{K_{IC}^2}{E}$ . The displacement loading is adopted, it is loaded step by step, and the increment of each loading is  $\Delta u_y = 1 \times 10^{-7}$  m. The computational domain is evenly divided, and the grid spacing is  $\Delta x = 1$  mm. In the PD region,  $\delta = 3\Delta x$ . The region division is shown in Fig. 10,  $L_1 = 49$  mm,  $L_2 = 85$  mm,  $L_3 = 3$  mm,  $L_4 = 46$  mm, and  $L_5 = 82$  mm.

Two crack angles are considered, i.e.  $45^\circ$  and  $62.5^\circ$ . The ultimate load can be obtained by calculating the sum of the nodal forces in the loaded circular hole. When the crack angle is  $45^\circ$ , the plate begins to damage when the load is about 2050 N. The ultimate failure load is about 2350 N, and the final crack paths are shown in Fig. 11a, which matches well with the experimental crack paths shown in Fig. 11b. For the crack with  $62.5^\circ$

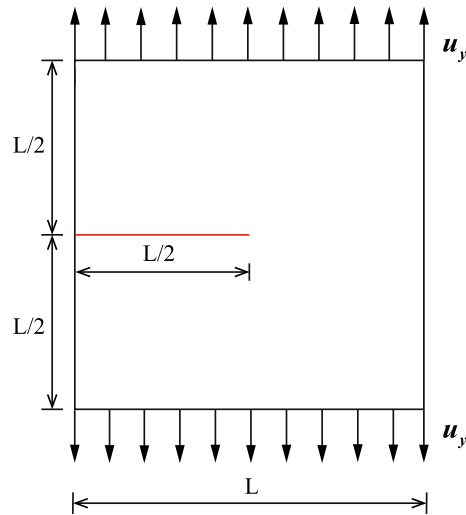


**Fig. 6** Schematic illustration of the square plate with an edge crack

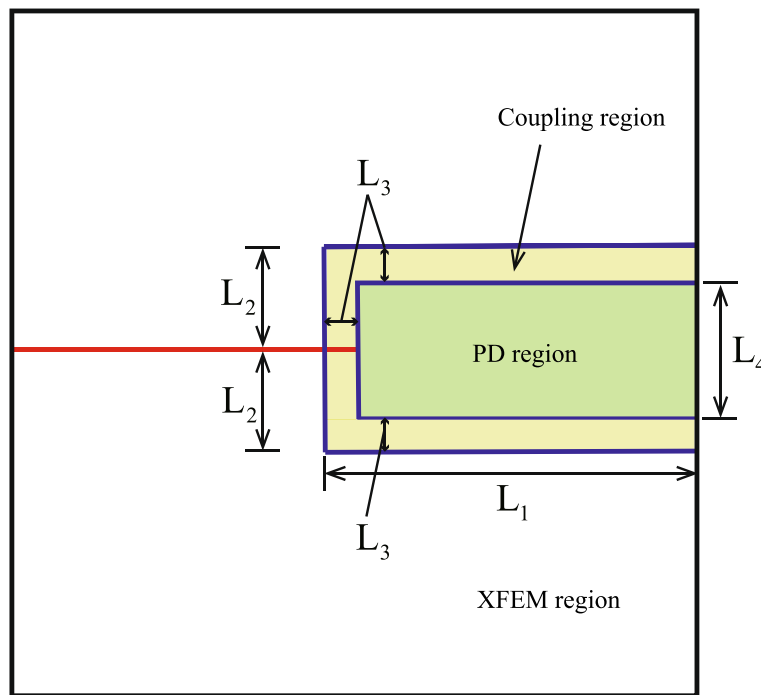


**Fig. 7** Schematic representation of sub-division of the computational domain into three regions

inclined angle, the crack grows when the load is about 2350 N, and the ultimate failure load is about 2900 N. The crack paths are shown in Fig. 12a, which agrees well with the path predicted in the experiment [37] shown in Fig. 12b. It is noted that the computed figures are rotated by 90° counterclockwise for comparing with the experimental results.

The ultimate failure loads obtained with the coupling method for the 45° crack and 62.5° crack are 2200 N and 2950 N, respectively. The average ultimate failure loads obtained with the experiment for the 45° crack and 62.5° crack are 2330 N and 3197.5 N [37], respectively. It is found that the ultimate failure loads obtained by the coupling method almost match with the experimental values.

The computational time is 38,333 s for the 45° crack and 45,973 s for the 62.5° crack using the coupling method. The computational time is 52,439 s for the 45° crack and 63,264 s for the 62.5° crack using the pure



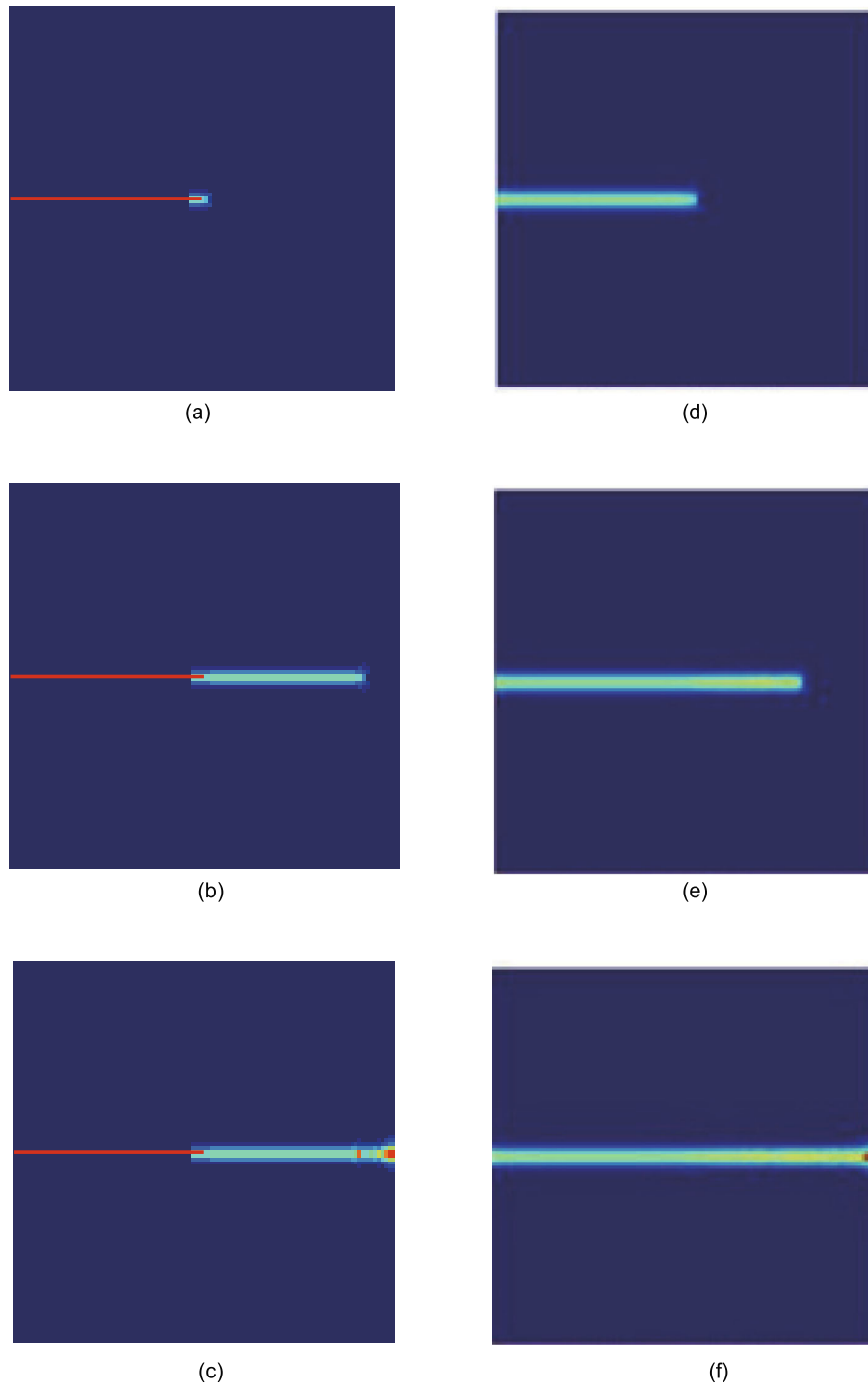


**Fig. 8** Crack propagation paths, **a–c** for the coupling method, and **d–f** for the pure PD

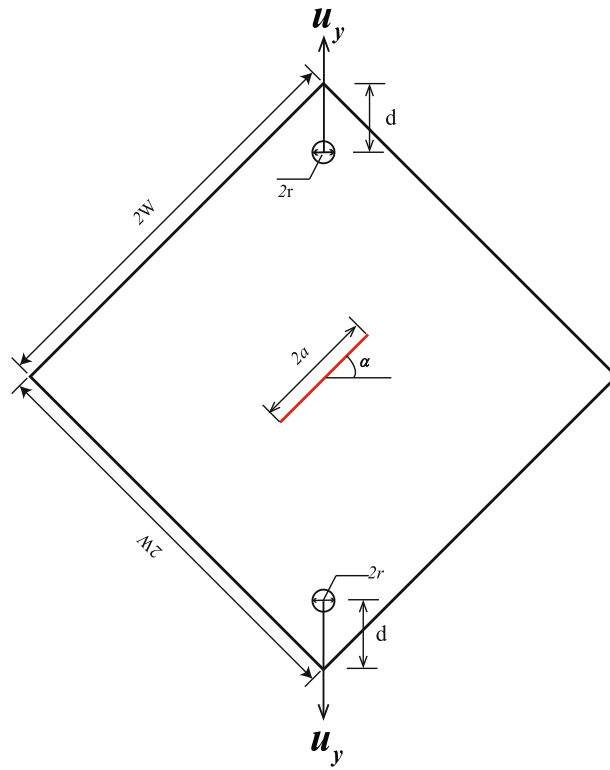


**Fig. 9** Schematic illustration of the plate with a central crack

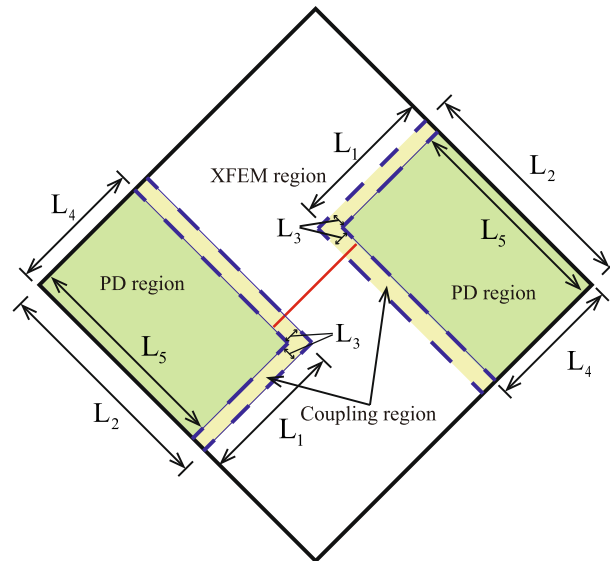


**Fig. 10** Region division of the plate with a central crack

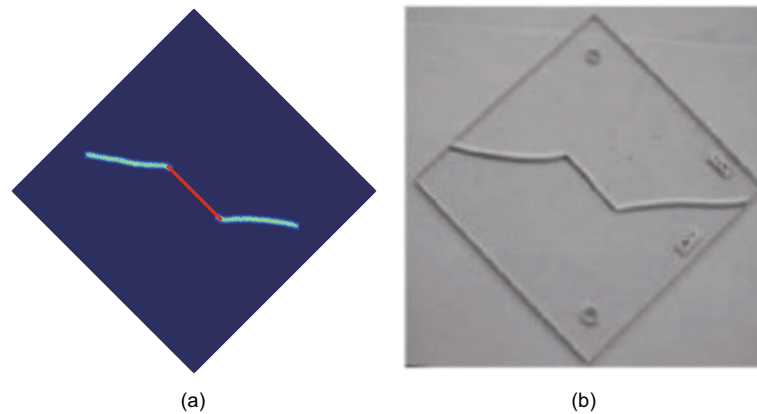


**Fig. 11** Comparison on the crack propagation paths for 45° crack between the present study (a) and the experimental data (b)

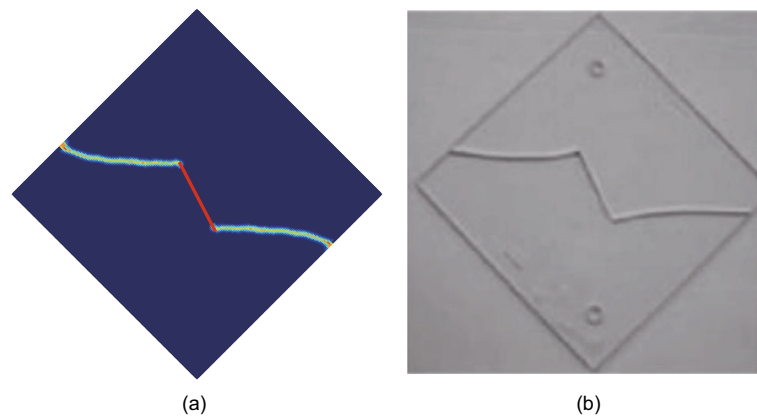


**Fig. 12** Comparison on the crack propagation paths for 62.5° crack between the present study (a) and the experimental data (b)

PD. This shows that the proposed framework can significantly improve the calculation efficiency compared with the pure PD.

#### 4.3 Dynamic crack propagation and branching in an edge-cracked plate

An edge-cracked plate subjected to uniaxial tension, as shown in Fig. 13, is simulated to verify the performance of the proposed framework for dynamic crack propagation problem. The plate length is  $L = 0.4$  m, the plate width is  $D = 0.1$  m, and the plate thickness is  $t = 0.001$  m. Young's modulus is  $E = 65$  GPa, Poisson's ratio is  $\nu = 0.2$ , material density is  $\rho = 2235$  kg/m<sup>3</sup>, and critical energy release rate is  $G_{IC} = 204$  N/m. The top and the bottom face is subjected to uniform pressure of  $P = 14$  MPa. The time integration step is  $\Delta t = 25$  ns, and the total computational time is 40  $\mu$ s.

The domain is divided into uniform grid, and two different spacing division methods are adopted, i.e.  $\Delta x = 1$  mm and  $\Delta x = 0.5$  mm. In the PD region,  $\delta = 3\Delta x$ . Figure 14 presents the schematic of the division of the computational domain into three regions. For  $\Delta x = 1$  mm,  $L_1 = 47$  mm,  $L_2 = 3$  mm, and  $L_3 = 50$  mm. For  $\Delta x = 0.5$  mm,  $L_1 = 48.5$  mm,  $L_2 = 1.5$  mm, and  $L_3 = 50$  mm. In order to prevent the loading boundary from being damaged first in the calculation process, the material points less than  $\delta$  from the upper and lower boundaries are set as non-destructive areas.

The crack paths obtained by the coupling method under two different discrete schemes and the pure PD [38] are represented in Fig. 15. It is found that the crack propagation and branching paths simulated by the proposed framework are almost consistent with crack paths obtained by the pure PD, but the crack paths for the coupling method with  $\Delta x = 0.5$  mm is more consistent with the results obtained by the pure PD. This shows that the coupling method has good convergence in solving the dynamic crack propagation problem.

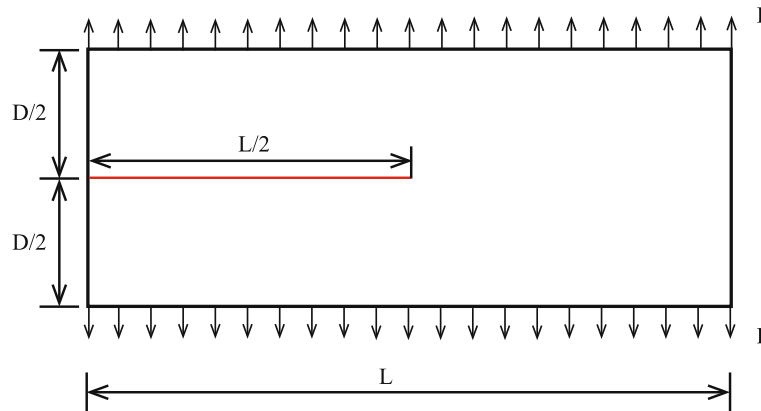


Fig. 13 Geometry model of the rectangle plate with an edge crack

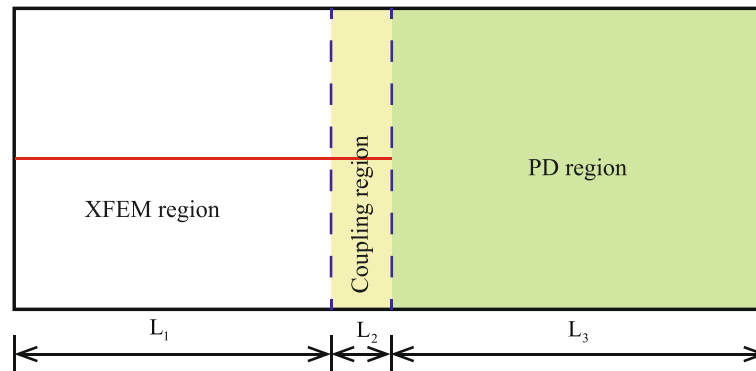


Fig. 14 Region division of the plate with an edge crack

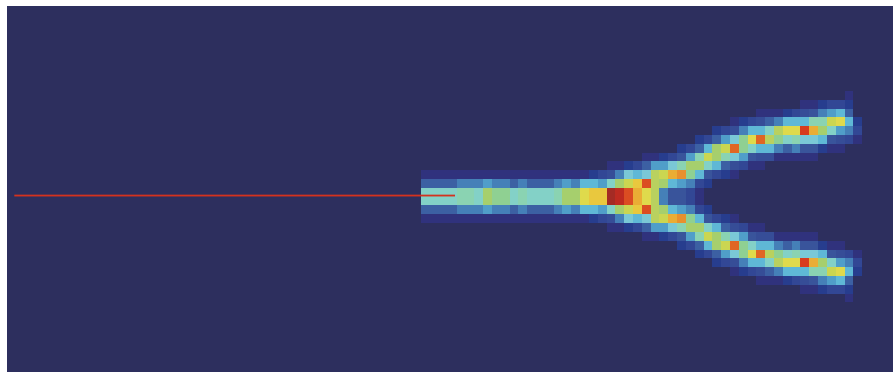
The crack propagation velocity is also an important index to measure the dynamic crack propagation. The fixed time interval  $\Delta t = 2 \mu\text{s}$  is adopted. Figure 16 shows the comparison of crack growth speeds of the coupled method under two different discrete schemes. It is obvious that the fluctuation of crack propagation speed decreases with the mesh refinement. In addition, the crack growth speeds obtained by the coupled method with  $\Delta x = 0.5 \text{ mm}$  are compared with those simulated by the PD, as shown in Fig. 17. The crack propagation speed curve of the coupling method is almost consistent with the results calculated by the PD, the maximum velocities of the crack propagation obtained from the coupling method, the PD and the experiment [38] are 1721 m/s, 1681 m/s and 1580 m/s, respectively. The Rayleigh wave velocity is about 3244 m/s, and the maximum crack growth velocity calculated by the coupling method is far less than the Rayleigh wave velocity, so the coupling method can also have high accuracy in the simulation of crack growth velocity.

#### 4.4 Simulation of Kalthoff–Winkler experiment

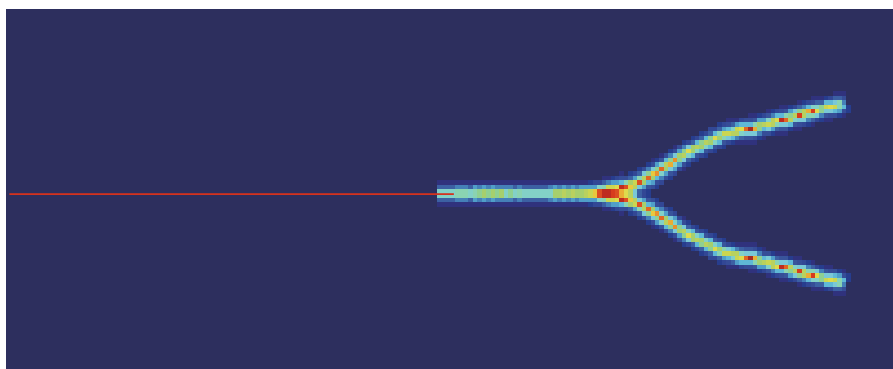
The last numerical example is devoted to simulation of dynamic crack growth for the Kalthoff–Winkler experimenting test. The details of geometry and boundary conditions of the Kalthoff–Winkler test are then shown in Fig. 18a. The impactor velocity is  $v_0 = 16.5 \text{ m/s}$ . Due to the geometric symmetry, only the upper part of the plate as shown in Fig. 18b is used for simulation. Young's modulus  $E = 190 \text{ Gpa}$ , Poisson's ratio  $\nu = 0.3$ , material density  $\rho = 8000 \text{ kg/m}^3$ , and critical energy release rate  $G_{IC} = 22170 \text{ N/m}$  are adopted. The time integration step is  $\Delta t = 50 \text{ ns}$ , and the total computational time is  $80 \mu\text{s}$ .

The grid is evenly divided, and the grid spacing is  $\Delta x = 1 \text{ mm}$ . In the PD region,  $\delta = 3\Delta x$ . Figure 19 represents the region division,  $L_1 = 0.047 \text{ m}$ ,  $L_2 = 0.003 \text{ m}$  and  $L_3 = 0.05 \text{ m}$ .

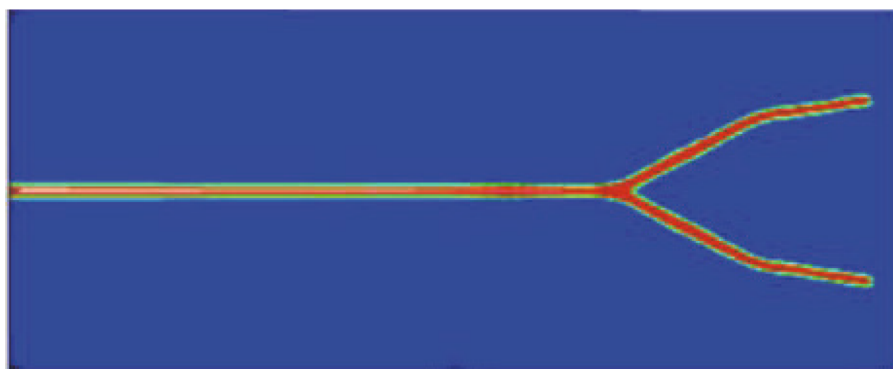
The crack paths obtained by the proposed framework are plotted in Fig. 20. The crack path results from the present approach are then compared with the reference crack paths derived from the XFEM. The crack path obtained by the coupling method extends linearly along the direction of  $65^\circ$ , which is consistent with the value



(a)



(b)



(c)

**Fig. 15** Crack propagation and branching paths, **a** coupling model for  $\Delta x = 1$  mm, **b** coupling model for  $\Delta x = 0.5$  mm, and **c** PD model

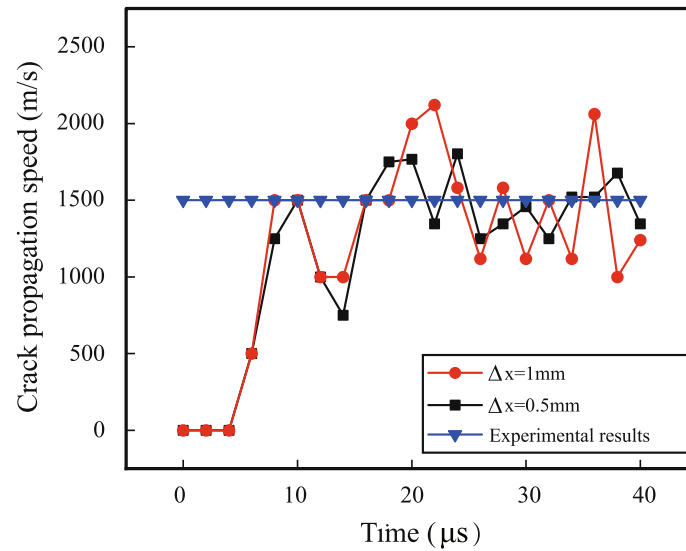


**Fig. 16** Comparison on crack propagation velocities for the coupling method with different discrete schemes

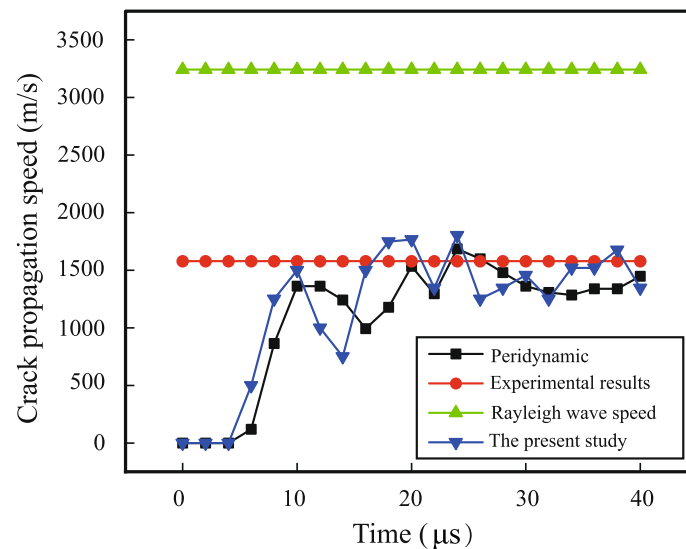


**Fig. 17** Comparison on crack propagation velocities for different methods

of  $67.5^\circ$  given in Ref. [39]. It shows that the proposed framework has good accuracy for simulating dynamic crack propagation problem.

The crack growth velocity is also investigated. The fixed time interval  $\Delta t = 2.5 \mu s$  is adopted. The Rayleigh wave velocity is  $CR = 2799.2$  m/s. In this analysis, the relative crack propagation velocity is defined as  $\frac{v}{CR}$ . Figure 21 shows the relative crack propagation velocity obtained by the coupling method, which is compared with the results obtained by the NOSB-PD [40], discrete method (DM) [41], 2D XFEM-PD [29] and discrete element method (DEM) [42]. In the coupling method, the crack growth starts at  $22.5 \mu s$ , and the propagation velocity is always much lower than that of Rayleigh wave speed. The results from the coupling method match well with those obtained by other numerical methods.

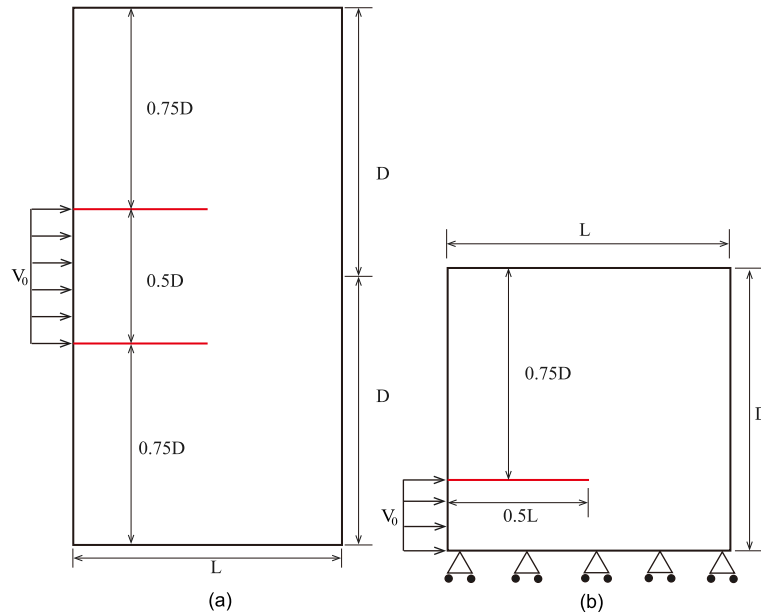


**Fig. 18** Geometry model of the rectangular plate, **a** the whole geometry model, and **b** the computational model

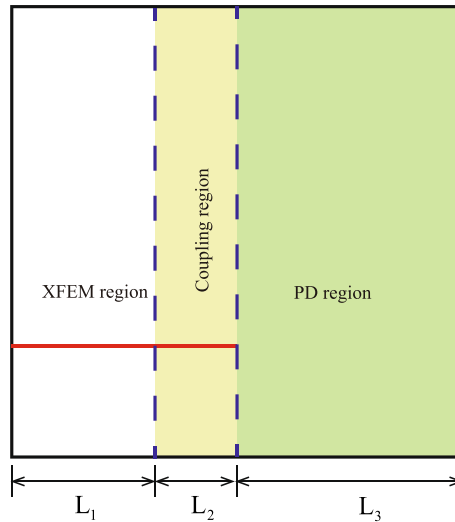
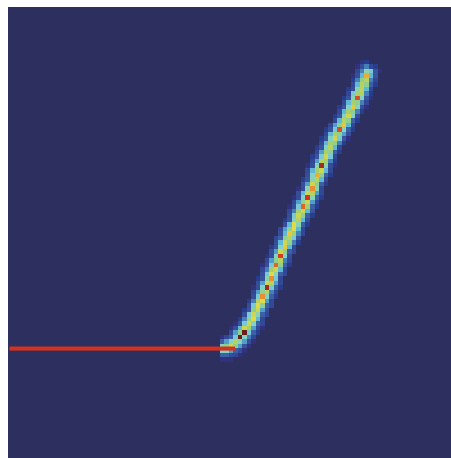


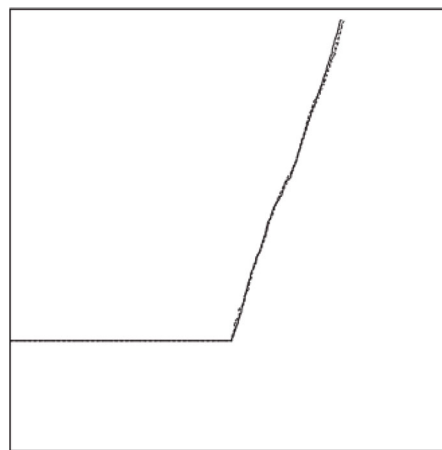
**Fig. 19** Region division of the rectangle plate

## 5 Conclusions

In this work, we have presented an efficient coupling approach between the XFEM and the state-based PD for two-dimensional crack propagation problems. Numerical simulations are accounted for fulfilling both the quasi-static and time-dependent dynamic boundary conditions. The SBPD is used in the vicinity of the crack tips and along the potential crack propagation regions, while the XFEM is adopted in the other regions. The coupling method has the advantages of the state-based PD and the XFEM, and can overcome the disadvantages of the two methods, so it can effectively simulate the crack propagation. The PD region remains unchanged in this study, and the potential crack propagation region is known in advance. A variable PD region can further save time, and this is a topic for future communication. The current development is flexible and has no limitation to solve other more complex problems such as fracture in three dimensions.



(a)



(b)

**Fig. 20** Comparison on the crack propagation paths between the coupling method (a) and the XFEM (b)

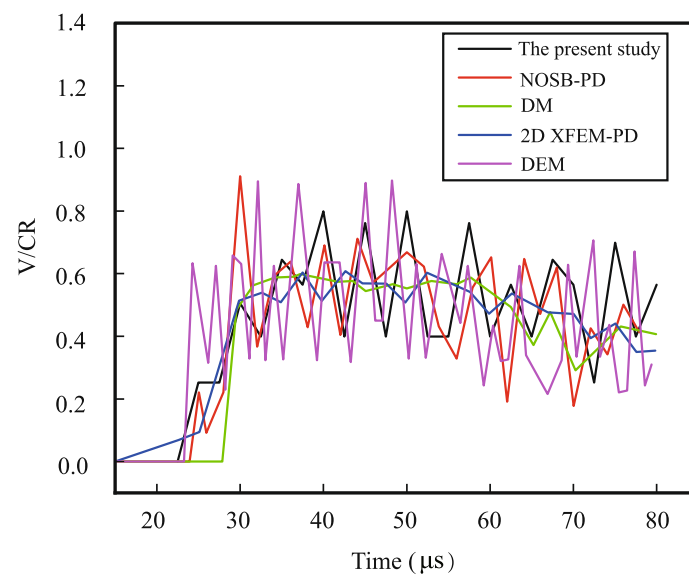


**Fig. 21** Comparison on the crack growth speeds amongst different methods



**Acknowledgements** This work is supported by the National Natural Science Foundation of China (Grant No. 11932006). The financial supports are gratefully acknowledged.

## Declarations

**Conflict of interest** The authors declare that they have no known competing financial interests or personal relationships that could have appeared to influence the work reported in this paper.

## References

1. Silling, S.A.: Reformulation of elasticity theory for discontinuities and long-range forces. *J. Mech. Phys. Solids* **48**(1), 175–209 (2000)
2. Diana, V., Carvelli, V.: An electromechanical micropolar peridynamic model. *Comput. Methods Appl. Mech. Eng.* **365**, 112998 (2020)
3. Gerstle, W., Sau, N., Silling, S.: Peridynamic modeling of concrete structures. *Nucl. Eng. Des.* **237**(12–13), 1250–1258 (2007)
4. Bazazzadeh, S., Morandini, M., Zaccariotto, M., Galvanetto, U.: Simulation of chemo-thermo-mechanical problems in cement-based materials with Peridynamics. *Meccanica* **56**, 2357–2379 (2021)
5. Huang, D., Zhang, Q., Qiao, P.: Damage and progressive failure of concrete structures using non-local peridynamic modeling. *Sci. China Technol. Sci.* **54**(3), 591–596 (2011)
6. Huang, D., Lu, G., Qiao, P.: An improved peridynamic approach for quasi-static elastic deformation and brittle fracture analysis. *Int. J. Mech. Sci.* **94**, 111–122 (2015)
7. Rabczuk, T., Ren, H.: A peridynamics formulation for quasi-static fracture and contact in rock. *Eng. Geol.* **225**, 42–48 (2017)
8. Gu, X., Zhang, Q.: A modified conjugated bond-based peridynamic analysis for impact failure of concrete gravity dam. *Meccanica* **55**(3), 547–566 (2020)
9. Ni, T., Zaccariotto, M., Zhu, Q., Galvanetto, U.: Static solution of crack propagation problems in Peridynamics. *Comput. Methods Appl. Mech. Eng.* **346**, 126–151 (2019)
10. Madenci, E., Barut, A., Futch, M.: Peridynamic differential operator and its applications. *Comput. Methods Appl. Mech. Eng.* **304**, 408–451 (2016)
11. Nowruzpour, M., Reddy, J.N.: Unification of local and nonlocal models within a stable integral formulation for analysis of defects. *Int. J. Eng. Sci.* **132**, 45–59 (2018)
12. Sarkar, S., Nowruzpour, M., Reddy, J.N., Srinivasa, A.R.: A discrete lagrangian based direct approach to macroscopic modelling. *J. Mech. Phys. Solids* **98**, 172–180 (2017)
13. Zhu, Q., Ni, T.: Peridynamic formulations enriched with bond rotation effects. *Int. J. Eng. Sci.* **121**, 118–129 (2017)
14. Li, W., Zhu, Q., Ni, T.: A local strain-based implementation strategy for the extended peridynamic model with bond rotation. *Comput. Methods Appl. Mech. Eng.* **358**, 112625 (2020)
15. Ni, T., Pesavento, F., Zaccariotto, M., Galvanetto, U., Zhu, Q., Schrefler, B.: Hybrid FEM and peridynamic simulation of hydraulic fracture propagation in saturated porous media. *Comput. Methods Appl. Mech. Eng.* **366**, 113101 (2020)
16. Liu, S., Fang, G., Liang, J., Fu, M.: A coupling method of non-ordinary state-based peridynamics and finite element method. *Eur. J. Mech. A Solids* **85**, 104075 (2021)
17. Littlewood, D. J.: Simulation of dynamic fracture using peridynamics, finite element modeling, and contact, In Proceedings of the ASME 2010 International Mechanical Engineering Congress & Exposition 44465 (2010) 209–217
18. Huang, X., Bie, Z., Wang, L., Jin, Y., Liu, X., Su, G., He, X.: Finite element method of bond-based peridynamics and its ABAQUS implementation. *Eng. Fract. Mech.* **206**, 408–426 (2019)
19. Fang, G., Liu, S., Fu, M., Wang, B., Wu, Z., Liang, J.: A method to couple state-based peridynamics and finite element method for crack propagation problem. *Mech. Res. Commun.* **95**, 89–95 (2019)
20. Yang, Y., Liu, Y.: Modeling of cracks in two-dimensional elastic bodies by coupling the boundary element method with peridynamics. *Int. J. Solids Struct.* **217–218**, 74–89 (2021)
21. Liang, X., Wang, L., Xu, J., Wang, J.: The boundary element method of Peridynamics. *Int. J. Numer. Meth. Eng.* **20**(122), 5558–5593 (2021)
22. Kan, X.Y., Zhang, A.M., Yan, J.L., Wu, W.B., Liu, Y.L.: Numerical investigation of ice breaking by a high-pressure bubble based on a coupled BEM-PD model. *J. Fluids Struct.* **96**, 103016 (2020)
23. Xia, Y., Meng, X., Shen, G., Zheng, G., Hu, P.: Isogeometric analysis of cracks with peridynamics. *Comput. Methods Appl. Mech. Eng.* **377**, 113700 (2021)
24. M. Behzadinasab, M. Hillman, Y. Bazilevs, IGA-PD penalty-based coupling for immersed air-blast fluid-structure interaction: a simple and effective solution for fracture and fragmentation, preprint [arXiv:2111.03767v1](https://arxiv.org/abs/2111.03767) (2021)
25. Behzadinasab, M., Moutsanidis, G., Trask, N., Foster, J.T., Bazilevs, Y.: Coupling of IGA and peridynamics for air-blast fluid-structure interaction using an immersed approach. *Forces Mech.* **4**, 100045 (2021)
26. Dorduncu, M., Barut, A., Madenci, E., Phan, N. D.: Peridynamic augmented XFEM, in: 58th AIAA/ASCE/AHS/ASC Structures, Structural Dynamics, and Materials Conference, 2017, p. 0656
27. Giannakeas, I.N., Papathanasiou, T.K., Fallah, A.S., Bahai, H.: Coupling XFEM and peridynamics for brittle fracture simulation-part I: feasibility and effectiveness. *Comput. Mech.* **66**(1), 103–122 (2020)
28. Giannakeas, I.N., Papathanasiou, T.K., Fallah, A.S., Bahai, H.: Coupling XFEM and Peridynamics for brittle fracture simulation: part II-adaptive relocation strategy. *Comput. Mech.* **66**(3), 683–705 (2020)
29. Liu, S., Fang, G., Liang, J., Lv, D.: A coupling model of XFEM/peridynamics for 2D dynamic crack propagation and branching problems. *Theoret. Appl. Fract. Mech.* **108**, 102573 (2020)

30. Chen, B., Yu, T., Natarajan, S., Zhang, Q., Bui, T.Q.: Three-dimensional dynamic and quasi-static crack growth by a hybrid XFEM-peridynamics approach. *Eng. Fract. Mech.* **261**, 108205 (2022)
31. Silling, S.A., Askari, E.: A meshfree method based on the peridynamic model of solid mechanics. *Comput. Struct.* **83**(17–18), 1526–1535 (2005)
32. Silling, S.A., Epton, M., Weckner, O., Xu, J., Askari, E.: Peridynamic states and constitutive modeling. *J. Elast.* **88**(2), 151–184 (2007)
33. Tong, Y., Shen, W.-Q., Shao, J.-F.: An adaptive coupling method of state-based peridynamics theory and finite element method for modeling progressive failure process in cohesive materials. *Comput. Methods Appl. Mech. Eng.* **370**, 113248 (2020)
34. Madenci, E., Oterkus, E.: *Peridynamic theory and its applications*. Springer, Berlin (2014)
35. Liu, P., Yu, T.T., Bui, T.Q., Zhang, C.: Transient dynamic crack analysis in non-homogeneous functionally graded piezoelectric materials by the X-FEM. *Comput. Mater. Sci.* **69**, 542–558 (2013)
36. Yu, T.: *Extended finite element method-theory, application and programming*. Science Press, Beijing (2014)
37. Ayatollahi, M., Aliha, M.: Analysis of a new specimen for mixed mode fracture tests on brittle materials. *Eng. Fract. Mech.* **76**(11), 1563–1573 (2009)
38. Ha, Y.D., Bobaru, F.: Studies of dynamic crack propagation and crack branching with peridynamics. *Int. J. Fract.* **162**(1), 229–244 (2010)
39. Zaccariotto, M., Mudric, T., Tomasi, D., Shojaei, A., Galvanetto, U.: Coupling of FEM meshes with Peridynamic grids. *Comput. Methods Appl. Mech. Eng.* **330**, 471–497 (2018)
40. Zhou, X., Wang, Y., Qian, Q.: Numerical simulation of crack curving and branching in brittle materials under dynamic loads using the extended non-ordinary state-based peridynamics. *Eur. J. Mech. A Solids* **60**, 277–299 (2016)
41. Braun, M., Fernández-Sáez, J.: A new 2D discrete model applied to dynamic crack propagation in brittle materials. *Int. J. Solids Struct.* **51**(21), 3787–3797 (2014)
42. Koteski, L., D’Ambra, R.B., Iturrioz, I.: Crack propagation in elastic solids using the truss-like discrete element method. *Int. J. Fract.* **174**(2), 139–161 (2012)

**Publisher’s Note** Springer Nature remains neutral with regard to jurisdictional claims in published maps and institutional affiliations.

Springer Nature or its licensor (e.g. a society or other partner) holds exclusive rights to this article under a publishing agreement with the author(s) or other rightsholder(s); author self-archiving of the accepted manuscript version of this article is solely governed by the terms of such publishing agreement and applicable law.